Identify Zr Promotion Effects at Atomic Scale for Co-based Catalysts in Fischer-Tropsch Synthesis

Yuang Piao, Qian Jiang, Hao Li, Jinsheng Liang, Hiroaki Matsumoto, Wei Liu, Cuong Pham-Huu, Yuefeng Liu, Fei Wang

Identify Zr Promotion Effects at Atomic Scale for Co-based Catalysts in Fischer-Tropsch Synthesis

Yuang Piao [a, b, ‡], *Qian Jiang* [b, ‡], *Hao Li* [c], *Jinsheng Liang* [a], *Hiroaki Matsumoto* [d], *Wei Liu* [b*], *Cuong Pham-Huu* [e], *Yuefeng Liu* [b *], *Fei Wang* [a*]

[a] Key Laboratory of Special Functional Materials for Ecological Environment and Information, Hebei University of Technology, Ministry of Education, Tianjin 300130, China

[b] Dalian National Laboratory for Clean Energy (DNL), Dalian Institute of Chemical Physics, Chinese Academy of Science, 457 Zhongshan Road, 116023 Dalian, China

[c] Department of Chemistry and the Oden Institute for Computational and Engineering Sciences, University of Texas at Austin, Texas 78712, United States.

[d] Hitachi High-Technologies (Shanghai) Co., Ltd, 201203, Shanghai, China

[e] Institute of Chemistry and Processes for Energy, Environment and Health (ICPEES), UMR 7515 CNRS-University of Strasbourg, 25 rue Becquerel, 67087 Strasbourg Cedex 02, France

ABSTRACT

Fischer-Tropsch synthesis (FTS) on cobalt-based catalysts are a vital route for converting syngas into high-value added long-chain hydrocarbons. Introducing promoters into the active phase is an efficient pathway for improving the catalytic performance and has been extensively studied. However, in the previous works devoted to the study of promoter effects the precise localization of the promoted active sites is seldomly investigated. The present work, for the first time, directly identify the chemical structure as well as the atomic location of promoter additive (e.g. ZrO_2) at atomic scale in the cobalt-based FTS catalysts under the wide molar ratio range of Zr/Co (from 0.12 to 1.5). Combining *in-situ*/*ex-situ* atomic resolution HAADF-STEM imaging and the related EDS elemental mapping and EELS analysis as well as physicochemical analyses (*in-situ* XRD, CO chemisorption, CO temperature programmed surface reaction, etc.) and FTS catalytic performance, it has been demonstrated that ZrO_2 promoter is presented as single-site dispersion on the surface of the Co nanoparticles (NPs) and the supports at low content, and further increase the Co NPs roughness which contributes to higher metallic surface area. Such isolated ZrO_2 species plays real active role to promote CO dissociation at the Co-ZrO_2 interface. While at high ZrO_2 content with Zr/Co molar ratio of 1.0 (ZrCo-1.0 catalyst), Zr is more inclined to nucleate on the surface of the support to form amorphous coating structure, whereas the rest still maintain mono-disperse on the surface of the Co nanoparticles. With further increasing the ZrO_2 content (the Zr/Co molar ratio up to 1.5), part of cobalt is encapsulated by ZrO_2 coating thus decreased the FTS activity. The *in-situ* EELS analysis and density functional theory calculations confirm

that Zr atom tends to bind the surface of Co NPs and the charge is transferred from Zr species to Co nanoparticle. The stronger interaction between Zr and cobalt in single site Zr-promoted Co catalyst could enhance the adsorbate binding with the H_2 molecule and the intermediate of the products as well as benefit CO dissociation. It thus displays the enhanced catalytic activity and long-chain hydrocarbon selectivity during the FTS reaction.

KEYWORDS: Fischer-Tropsch synthesis, cobalt nanoparticle, ZrO_2, single-site promoter, atomic resolution STEM

TOC

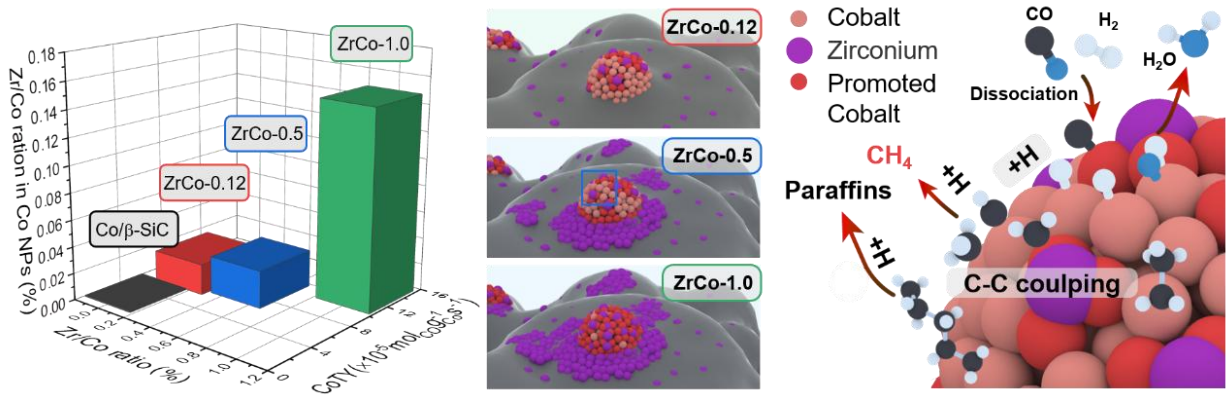

Introduction

The metal-based catalysts in heterogeneous catalysis generally require the promoters, such as noble metals, transition metal oxides or rare earth metal oxides, to attain the optimized catalytic performance.[1-2] The intimate contact between active metal and promoter is essential for the catalysis, resulting in the modulation of metal-promoter interaction as an efficient strategy to enhance the catalytic performance.[3-5] To date, extensive researches have been devoted to developing the promoters for cobalt-based FTS catalyst[6-8], which is considered as an ideal choice for the synthesis of long-chain products (C_{5+}) like gasoline and diesel via syngas.[9] The addition of noble metal promoters (*e.g.* Pt) generally promotes the degree of reduction of Co and may further enhance the dispersion of Co or even improve the C_{5+} selectivity by increasing the probability of α-olefins re-adsorption.[8, 10-12] While considering the cost control for industrial FTS process and limited reserves for the noble metals, transition metal oxides promoters, such as MnO_x and ZrO_2 as typical, have been widely studied for enhancing the catalytic activity, C_{5+} selectivity and suppress the CH_4 production through CO methanation reaction.[13-15] For example, Morales et al.[14] reported that Mn promoted Co/TiO_2 display a rise in C_{5+} selectivity and a decrease in CH_4 selectivity. They proposed that the interaction between Co-Mn and solid-solution spinel compound formed in the calcined catalyst that leads to the shift of products selectivity.

It is reasonable that ZrO_2 could play as structure promoter to inhibit the strong metal-support interaction between Co and industrial active oxide supports (*e.g.* Al_2O_3) and the formation of $CoAl_2O_4$ mixture oxide. [16-20] When the interaction between Co and inert oxide support (*e.g.* SiO_2)

has been replaced by that of Co and ZrO_2, the Co dispersion is increased and thus the activity and the product selectivity could be promoted.[21-22] The main conclusions in aforementioned works suggest the interaction between Co and support could be moderated by the introduction of ZrO_2, resulting better reducibility of Co species, the highly exposed metallic active sites and thus the improved FTS activity.[23] Moreover, the interface of ZrO_2 and Co could also enhance the CO dissociation according to work from Jr. Goodwin.[20] A.T. Bell and co-workers reported the intrinsic promotion role of ZrO_2 on Co-based FTS catalyst for the improved catalytic activity and C_{5+} selectivity.[24] Combing the *in-situ* X-ray absorption spectroscopy with kinetics experiments, it has been clarified that the interface between ZrO_2 and Co nanoparticles increases since the Co nanoparticles are partly covered by ZrO_2 and then the fraction of active sites adjacent to the ZrO_2 species are enhanced. Although the developments concerning the ZrO_2 promoter on Co-based FTS catalysts have been well achieved by using numerous spectroscopic techniques/methodologies,[17, 23] the direct evidences of structural origin at atomic-scale of the metal oxide promoters (*e.g.* ZrO_2) on the Co-based FTS catalyst are still missing. In particular, the atomic-scale structural and compositional information of ZrO_2 under the low or high doping concentration is not well identified and thus the structure-activity relationship of the catalysts with the influence of the promoters is still lacking.

With the advanced development of electron microscopy in the last few decades, especially with the aid of the aberration-corrected (AC)-STEM, the atomic arrangement of complex catalyst system could be investigated directly to get the depth insight in the relationship of structure and catalytic activity. [25-28] Herein, the interactions between the added promoter and the metal or the

support are investigated systematically by using the *in-situ* and *ex-situ* AC-STEM combined with energy disperse spectroscopy (EDS) and electron energy loss spectroscopy (EELS) as well as chemisorption experiments. Various promoter concentrations of ZrO_2 promoted Co catalysts were prepared with the atomic ratio of Zr/Co varying from 0.12 to 1.5. It is worth noting that the chemical properties of the ZrO_2 promoted Co catalytic system are well identified previously[24] and thus render us the effective observation of the atomic nature of the metal-promoter interaction by using AC-STEM and atomic scale electron spectroscopies (EDS and EELS). Furthermore, the chemical inert and thermal conductive porous β-SiC was chosen as support for facilitating the heat dispersion since the strong exothermic property of FTS reaction. [29-34]

Experimental Methods

2.1 Catalyst preparation

Cobalt based catalysts were prepared by incipient co-impregnation of porous β-SiC (provided by SICAT Corporation) using aqueous solutions of $Co(NO_3)_2 \cdot 6H_2O$ (Alfa Aesar, 98%-102% purity) and $ZrO(NO_3)_2$ (Sigma-Aldrich, 99.999% purity). The solution concentration was adjusted to achieve the targeted Zr/Co atomic ratio at a Co loading of 10 wt%. After impregnation, the catalyst was aged at room temperature for 4 hours and then dried at 110 °C for 12 hours followed by the calcination in a Muffle furnace at 350 °C for 3 hours with a heating rate of 2 $°C \cdot min^{-1}$ unpromoted catalyst is denoted as Co/β-SiC. Zr promoted cobalt based catalysts are named according to the Zr/Co atomic ratio (0.12, 0.5, 1.0, and 1.5), which are abbreviated as ZrCo-*x*, x = 0.12, 0.5, 1.0, and 1.5. ZrO_2 supported catalyst is also prepared as the reference

sample, which is named as Co/ZrO_2. The other two catalysts for comparison were prepared by step impregnation method with the constant Zr/Co atomic ratio of 1.0. First step was to impregnate the aqueous solution of the $ZrO(NO_3)_2$ into porous β-SiC. After aged at room temperature for 4 hours and dried at 110 °C for 12 hours, the precursor was calcinated in a Muffle furnace at 350 °C and 650 ^{o}C, respectively, for 3 hours with a heating rate of 2 °C·min^{-1}. The samples were then impregnated with aqueous solutions of $Co(NO_3)_2{\cdot}6H_2O$ through the same procedure, and the calcination temperature was fixed at 350 °C. The catalysts are named according to the calcination temperature of Zr- containing precursor (350 °C and 650 °C), which are abbreviated as $Co@Zr_{350}$-1.0 and $Co@Zr_{650}$-1.0.

2.2 Catalyst evaluation

Fischer-Tropsch reaction was carried out on a home-made three-channel fixed bed setup with the temperature controlled by one oven. The catalysts were loaded into a quartz tube inside the stainless-steel reactor to avoid the influence of metal impurity. The reaction temperature was monitored by thermocouples inserted into the catalyst bed. The gas flow through the fixed bed reactor was regulated by mass flow controller and the pressure was regulated by back pressure regulator. Two traps were designed to collect liquid and wax products where the hot trap was maintained at 100 °C and the cold trap at 0 °C. The gas phase products were analyzed by an online Agilent 7890B gas chromatograph equipped with TCD and FID detector. The non-gasous products were collected after reaction and analyzed by an Agilent 7820A gas chromatograph offline.

The catalyst with the particle size of 160-400 μm diluted with 2 g SiC (particle size ca. 350 μm) was loaded in the middle of the reactor in the isothermal zone to avoid problems linked with inhomogeneous temperature gradient. Prior to reaction, the catalyst was reduced in 60 $mL \cdot min^{-1}$ H_2 at 350 °C for 8 hours with a heating rate of 2 ° $C \cdot min^{-1}$ at atmospheric pressure. Then it was cooled down to 210 °C and flashed with Ar for 1 hour to remove the H_2 in the system. Afterward, the pressure was raised to 20 bar. When the temperature and pressure is stable, syngas (H_2/CO=2, N_2 as internal standard) was introduced into the reactor. Considering the strong exothermic character of the Fischer-Tropsch synthesis, a very low heating rate, i.e. 1° $C \cdot h^{-1}$ was utilized during increasing to the target reaction temperature of 220 ° C. The reaction was maintained at 220 ° C and 20 bar for 4 days. Notably particularly, the syngas was introduced into the reactor at the same reaction condition for 25 hours before the data was acquired to stabilize the reaction.

The cobalt time yield (CoTY) was calculated based on molar CO consumption per gram cobalt per second.

$$CoTY(\times 10^{-5} mol_{CO} \cdot g_{Co}^{-1} \cdot s^{-1}) = \frac{F_{CO,in} - F_{CO,out}}{m_{Co}}$$

$F_{CO, in}$ and $F_{CO, out}$ represent flow rate of CO in the feed gas and CO in the effluent in the unit of $mol \cdot S^{-1}$. m_{Co} represents the mass of Co in the catalyst.

C_{5+} selectivity was calculated as following,

$$C_{5+} = (1 - \frac{\sum_{i=1}^{4} F_{\mathrm{out},C_i}}{F_{CO,in} - F_{CO,out}}) \times 100\%$$

The carbon balance was calculated by following equation,

$$X_C = \frac{\sum_{i=1}^{7} n_{\text{gas,out},C_iH_x} + \sum_{i=6}^{24} n_{\text{cold-trap},C_i} + \sum_{i=7}^{42} n_{\text{hot-trap},C_i} + F_{CO,out} * t}{F_{CO,in} * t}$$

$\sum_{i=1}^{7} n_{\text{gas,out},C_iH_x}$, $\sum_{i=6}^{24} n_{\text{cold-trap},C_i}$ and $\sum_{i=7}^{42} n_{\text{hot-trap},C_i}$ represent the amount of the gas phase, oil phase and wax phase. t represents the reaction time, which is calculated when the furnace temperature reached 220 ° C. The carbon balance of all tested catalysts is in the range of 95±5%.

2.3 Catalyst Characterization

The powder X-ray diffraction (XRD) patterns were recorded on an X'pert-Pro diffractometer (PAN Analytical, Netherlands) using Cu Kα radiation at 40 kV and 40 mA in the range of 10°-80° using the step size of 0.2 degree. The catalysts after the reaction were collected from diluting agent by screening and were subject to XRD characterization immediately. The in situ XRD is also recorded on an X'pert-Pro diffractometer in the range of 30° -50° using the step size of 0.12 degree. The flow rate of H_2 is 30 mL·min^{-1}, the heating rate is 5 ° C·min^{-1}, and from 160 ^{o}C the temperature is kept 20 min every 20 ^{o}C for measuring the patterns. When the temperature was raised to 350 ^{o}C, the reduction was continued for 2 hours.

The specific surface area, pore volume and the average pore diameter of the samples were measured by N_2 physisorption on Micromeritics ASAP 2020 apparatus working at -196 °C. Before measurement, the samples were degassed under vacuum at 180 °C for 6 hours. The specific surface area was calculated according to the multipoint Brunauer-Emmett-Teller (BET) method. The pore volume and average pore diameter were calculated using the Barrett-Joyner-Halenda (BJH) method with desorption branch of the isotherms.

The temperature-programmed reduction (TPR) was conducted in a fixed bed reactor with a U shape quartz tube (inner diameter 6 mm) at atmospheric pressure monitored by a Pfeiffer Omni star mass spectroscopy. Firstly 50 mg sample was heated to 100 °C under the flow of 99.99% He (40 $mL \cdot min^{-1}$) with the ramp of 10 $°C \cdot min^{-1}$, and held for 1 hour to eliminate H_2O and impurity until stable baseline was obtained. Then it was heated to 800 °C under the flow of 5% H_2/He (40 $mL \cdot min^{-1}$) with a heating rate of 5 $°C \cdot min^{-1}$. The mass signals of m/z = 17 was used to record the as generated H_2O during the reduction process.

The temperature programmed desorption of NH_3 (NH_3-TPD) was performed to characterize the acidity of samples on Micromeritics AutoChem 2910. Prior analysis 100 mg sample was reduced at 350 °C under 5% H_2/He for 2 hours. Afterwards the reactor temperature was cooled down to room temperature and 40 $mL \cdot min^{-1}$ of 10% NH_3/He was passed through the sample for 2 hours during adsorption followed by He purge to remove the physically adsorbed NH_3. Then the sample was heated to 700 °C under the flow of 99.99% He with a heating rate of 10 $°C \cdot min^{-1}$. The mass signal of m/z = 15 was used to record the NH_3 desorbed.

To understand the behaviors for CO adsorption and activation for different catalysts, the CO temperature programmed desorption experiments were performed with the signals recorded by mass spectroscopy. 50 mg catalyst was reduced at 350 °C under pure H_2 (40 $mL \cdot min^{-1}$) for 4 hours and then the gas was switched to He to purge the adsorbed H_2 for 30 min followed by cooling down to 50 °C. Afterwards, pure CO (40$mL \cdot min^{-1}$) was introduced for adsorption at 50 °C for 30 min in the reactor. The reactor was purged with He for 1 hour to remove the physically adsorbed CO until baseline stable. The sample was heated from 50 °C to 700 °C at a

ramp of 10 °C·min^{-1} using the mass signal of m/z of 28 was continuously recorded for CO evolving. In the same device, the reactivity of surface metallic cobalt was evaluated by CO temperature programmed surface reaction (CO-TPSR). The reduction and CO adsorption procedures are the same as those used for CO-TPD mentioned above. The temperature programmed reaction process was conducted with 30 mL gas flow of 5% H_2/He heated from 50 to 800 °C at a rate of 10 °C·min^{-1}. The mass signal of m/z = 15 was monitored for the CH_4 formed.

2.4 Transmission electron microscopy analysis

Aberration corrected high-angle annular dark-field scanning transmission electron microscopy (HAADF-STEM) was performed on a JEOL JEM-ARM200F microscope. The elemental composition as well as distribution were analyzed on the energy dispersive X-ray analyzer (EDS, EX-230 100 m^2 detector) equipped on the microscope. The sample was ultrasonicated in ethanol solution and a drop was deposited on a copper grid covered with a holey carbon membrane. The catalyst was reduced under 5% H_2/He for 8 hours followed by a passivation in 0.5% O_2/He to protect Co particles from excessive oxidation before the microscopy characterization.

In-situ STEM analysis and EELS spectrum was performed on a newly developed HF5000 microscope from the Hitachi Company with a 200 kV cold-field emission gun and a Cs-corrector for the electron probe. The catalysts Co/β-SiC and ZrCo-1.0 was reduced in *ex-situ* condition at 350 ° C for 8h under H_2 flow (40 mL·min^{-1}) followed by passivation in 0.5% O_2/He to protect cobalt particles from excessive oxidation in laboratory. The in-situ experiment was initiated via a

MEMS-based heating method (using a MEMS compatible holder designed by Hitachi Company). Afterwards, the samples were deposited on holder and reduced in microscopy under 500 ° C in H_2 atmosphere (P=2 Pa). Maintaining the temperature and atmosphere when collected STEM images and EELS spectra.

2.5 Computational and modeling methodology

Spin-polarized density functional theory (DFT) calculations were performed using the VASP code. The core electrons were described by the projector augmented-wave method.[35] The electronic exchange and correlation were described by a generalized gradient approximation method using the Perdew–Burke–Ernzerhof functional.[36] The valence electrons were described by the Kohn–Sham wave functions being expanded in a plane-wave basis with the energy cutoff of 400 eV. [37] Brillouin zone was sampled with (3×3×1) Monkhorst–Pack *k*-point mesh.[38] For convergence, all the configurations were defined as optimized when the forces of each atom fell below 0.05 eV/Å. The Co surface was modeled as a 4-layer, 4×4, (111) surface, with the lattice constant of 3.53 Å.[39] The bottom two layers were fixed in bulk position, while the rest of the layers were allowed to relax. To model different atomistic environments of Zr, Zr-in-Co(111) and Zr-on-Co(111) were modeled, which respectively represent the Zr inside and outside of the Co lattice. The Zr-in-Co(111) was modelled by replacing a surface Co with a Zr, while the Zr-on-Co(111) was modelled by placing a Zr atom on a Co(111) surface. The H, C, and CO binding energies were calculated respectively using the total energies of H, C, and CO (in vacuum) as the references.

Results

FTS activities

The FTS catalytic performances of the prepared samples with different Zr/Co molar ratios (Zr/Co molar ratios of 0, 0.12, 0.5, 1.0 and 1.5) are evaluated. The results (Figure 1a) show that the catalysts present superior stability and the CoTY value (Cobalt time yield, molar CO conversion per gram cobalt per second) does not significantly decrease along with time on stream. Surprisingly, the ZrCo-0.12 sample with ultra low ZrO_2 concentration (2.1 wt%) presents more than 2-fold CoTY value (8.4×10^{-5} mol_{CO} g^{-1}_{Co} s^{-1}) compared to that of Co/β-SiC (3.3×10^{-5} mol_{CO} g^{-1}_{Co} s^{-1}), demonstrating the positive contribution of ZrO_2 additions. With further increase of the Zr/Co molar ratio (Figure 1b), the CoTY gradually increases to the 12.8×10^{-5} mol_{CO} g^{-1}_{Co} s^{-1} over Zr/Co-1.0 sample and subsequently decreases to 7.9×10^{-5} mol_{CO} g^{-1}_{Co} s^{-1} over Zr/Co-1.5 and 3.9×10^{-5} mol_{CO} g^{-1}_{Co} s^{-1} over pure ZrO_2 supported cobalt catalyst (Co/ZrO_2). The highest FTS activity on ZrCo-1.0 catalyst is 7-fold higher than that of unpromoted catalyst (Co/SiC), where the ZrO_2 concentration is 20 wt%. It is worth noting that the increment degree of FTS activity is not linear correlation with the addition amount of ZrO_2, where 10% and 50% increment degree for CoTY when increment degree of zirconium atoms content is 0.5 and 1.0, respectively, for ZrCo-0.12 to ZrCo-0.5 and to ZrCo-1.0. The results reveal that the role of Zr promotion effects is rather different along with the different ZrO_2 loading.

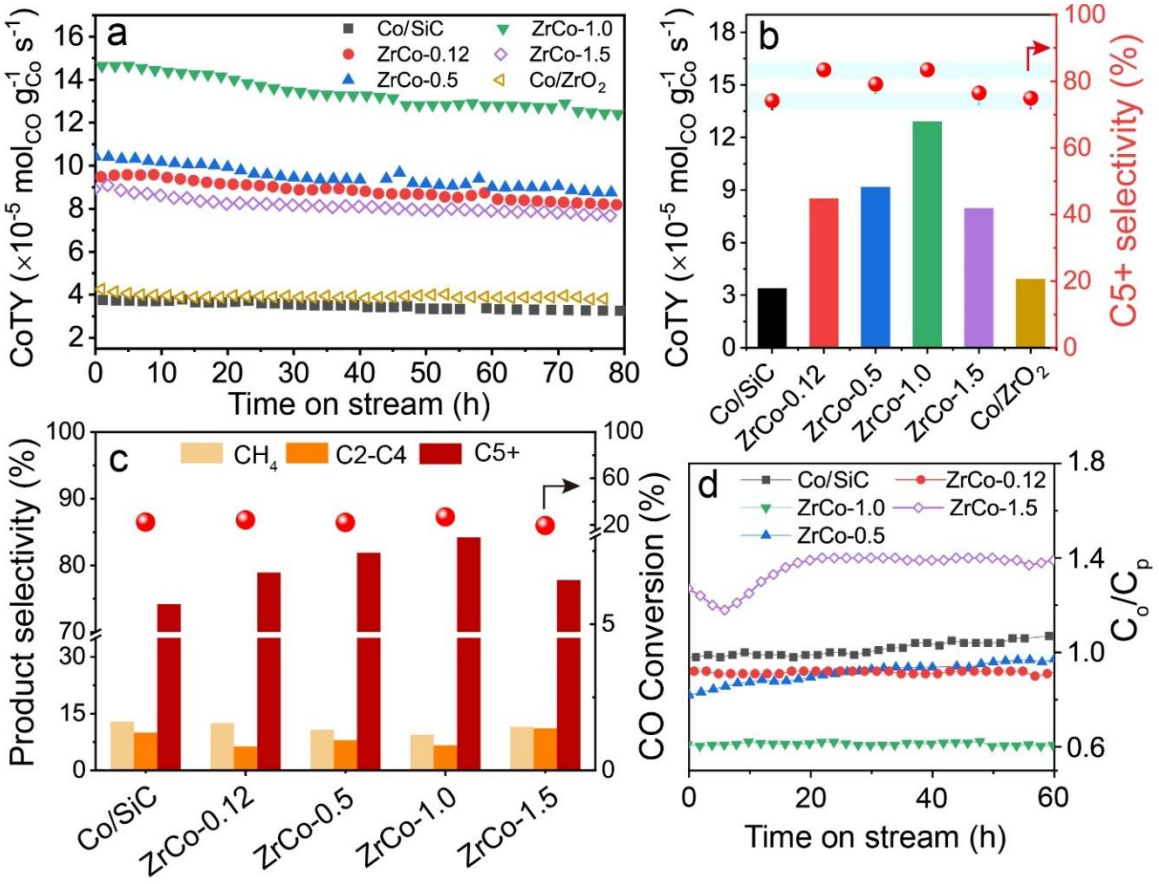

Figure 1. (a) FTS catalytic performance as a function of time on stream and (b) the average value of CoTY (columns) and C_{5+} selectivity (dots) in the time range of 20-80 h. Reaction conditions: H_2/CO molar ratio = 2, pure syngas, reaction temperature = 220 °C, total pressure = 20 bar, GHSV (STP) = 4800 mL h^{-1} g_{cat}^{-1} for Co/SiC, ZrCo-0.12, ZrCo-1.5 and Co/ZrO_2; GHSV (STP) = 12,000 mL h^{-1} g_{cat}^{-1} for ZrCo-0.5 and ZrCo-1.0. (c) Product selectivity and (d) C_2-C_4 olefin/paraffin ratio (Co/Cp) as a function of time on stream under the similar CO conversion (around 20%). Reaction condition: GHSV (STP) = 4800 mL h^{-1} g_{cat}^{-1} for Co/SiC and ZrCo-1.5 GHSV (STP) = 12,000 mL h^{-1} g_{cat}^{-1} for ZrCo-0.12 and ZrCo-0.5; GHSV (STP) = 18,000 mL h^{-1} g_{cat}^{-1} for ZrCo-1.0

The ZrO_2 introduction also influences the C_{5+} selectivity (Figure 1b). The ZrCo-0.12 catalyst with small amount of ZrO_2 introduction shows higher C_{5+} selectivity (85%) compared to that of Co/SiC catalysts (72%), which due to the presence of ZrO_2 near the Co nanoparticle benefits C-C coupling.[24] While further increase the Zr content as to catalyst ZrCo-1.5, the C_{5+} selectivity decreases to 76%, with the similar level as pure ZrO_2 supported catalyst and Co/SiC. To shed light on the influence of ZrO_2 promotion for the product selectivity, the GHSV was adjusted to maintain the CO conversion at around 25% for all investigated ZrCo-*x* catalysts. The products selectivity of CH_4, C_2-C_4 and C_{5+}, as well as the C_2-C_4 olefin/paraffin ratio (C_o/C_p) are presented in Figures 1c, 1d, S1 and S2. The C_{5+} selectivity of ZrCo-*x* catalyst increases with the increment of Zr/Co ratio and reach to 84.2 % at maximum value for ZrCo-1.0 catalyst and subsequently decrease to the 77.8% for ZrCo-1.5 catalyst. The increase in the selectivity of the C_{5+} product could attribute from the improvement of hydrogenation ability by adding the Zr species, which also result in the lower C_2-C_4 olefin/paraffin ratio (Figure 1d). The trend is consistent with the early reports of Feller et al.[16], whereas different from the reports from Johnson et al.[24] and Moradi et al.[17] that the C_{5+} selectivity increases along with ZrO_2 addition and reach the selectivity plateau at higher ZrO_2 loading. Moreover, these thermally conductive porous β-SiC supported ZrCo-*x* catalyst presents the FTS catalytic performance superior to the most of reported zirconium promoted cobalt catalysts (Table S1).

Physicochemical characteristics of supported CoZr-*x* catalysts

The XRD patterns for calcined β-SiC supported catalysts are presented in Figure 2a. The β-SiC support presents three main diffraction peaks at 35.5° , 59.9° and 72.2° corresponding to (111), (220) and (311) planes, respectively. The additional diffraction peaks emerge at 36.8° , 31.3° and 65.2° after Co introduction, which are attributed to (311), (220) and (440) planes of Co_3O_4. As shown in Table 1 and Figure 2a, the Zr introduction brings no significant influence on the crystal phase composition of the catalyst in aspects of either Co_3O_4 dispersion or the new phase formation even when the Zr content is as high as 20 wt%, which indicates that the Zr species are well dispersed in sub-nano sizes or in amorphous phase without contributing periodic diffraction contrast.

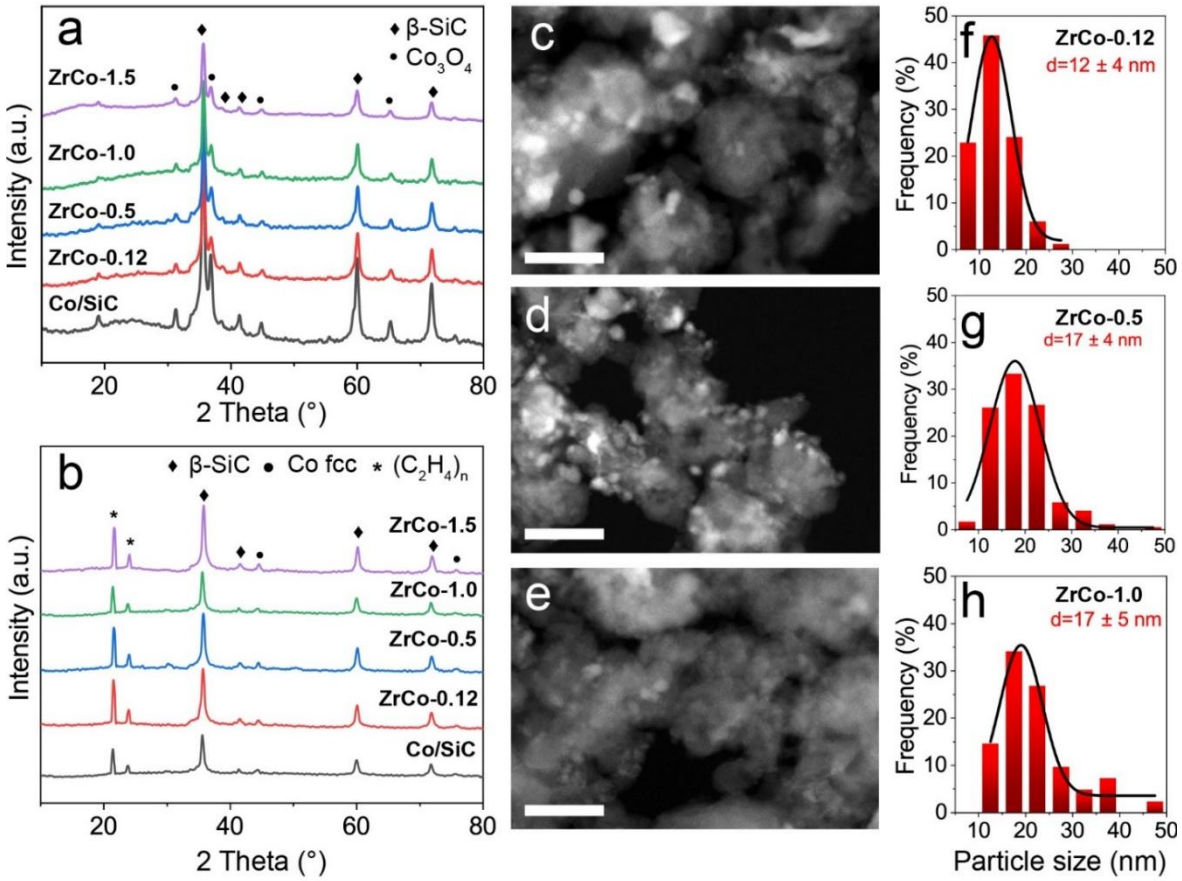

Figure 2. XRD patterns for calcined catalysts (a) and catalysts after 80 hours FTS reaction (b). HAADF-STEM images (scale bar 100 nm) and the corresponding particle size distribution for passivated ZrCo-0.12 (c, f), ZrCo-0.5 (d, g) and ZrCo-1.0 (e, h)

The XRD patterns of spent catalysts show some apparent new diffraction peaks located at about 21° and 23°, attributed to $(C_2H_4)_n$ for the products in oil and wax phase (Figure 2a). The diffraction peaks at 44.4° and 75.8° attribute to the (111) and (220) planes of metallic Co in fcc (face-centered cubic) phase. There still no obvious change of the cobalt crystallite size with various ZrO_2 concentrations, which suggests that Zr promoter slightly influences the cobalt crystallite size and dispersion during the reaction. The HAADF-STEM images and particle size distribution of passivated ZrCo-*x* catalysts (Zr/Co = 0.12, 0.5 and 1.0) are shown in Figure 2 The cobalt particle size of ZrCo-0.12 is 14 nm, which is slightly smaller than that of ZrCo-0.5 (17 nm) and ZrCo-1.0 (17 nm). However, the crystallite size of cobalt for all ZrCo-*x* catalysts become larger in a certain extent after FTS reaction (Table 1), which is mainly due to the sintering occurs in the test due to the relative weak metal-support interaction by using chemical inert SiC support.[31, 34]

In-situ XRD experiment of ZrCo-1.0 catalyst was conducted during the reduction process to investigate the effects of Zr species on the microstructure of cobalt NPs. It can be clearly seen that the as-prepared ZrCo-1.0 catalyst had significant Co_3O_4 diffraction peaks, but not the zirconium-related diffraction peak, indicating the ZrO_2 only presented in the amorphous state. As

shown in *in-situ* XRD patterns in Figure 3b, the diffraction peak of Co_3O_4 start to disappear and a CoO (200) peak (42.4°) emerges when the reduction temperature increases from room temperature to 250 °C. When the temperature reaches 350 °C, the diffraction peak of CoO gradually disappears, replaced by that of metallic Co (111) at diffraction peaks of 44.4°. The *in-situ* reduction was then maintained at 350 °C for 2 hours. It is found that the CoO diffraction peak completely disappeared, and the FWHM of the Co diffraction peak gradually increased, indicating that Co particles gradually formed during the reduction process. The *in-situ* XRD results are consistent with the two-step reduction characteristics of Co_3O_4 in the previous literature[40]. Although in presence of ZrO_2 on the ZrCo-1.0 catalyst, the diffractions (lattice spacings) of Co phase do not exhibit a visible shift, and no diffraction peak of Zr species is detected during the reduction process, which further confirmed that Zr species are in either mono-atom dispersion or the amorphous form in the Zr-Co catalyst without contributing any periodic diffraction. Furthermore, the *ex-situ* XRD patterns for passivated Co/SiC and ZrCo-1.0 were directly compared (Figure S4). The results also clearly show no peak shifting for metallic Co diffraction peak over ZrCo-1.0 catalyst compared to that of unpromoted Co/ SiC catalyst.

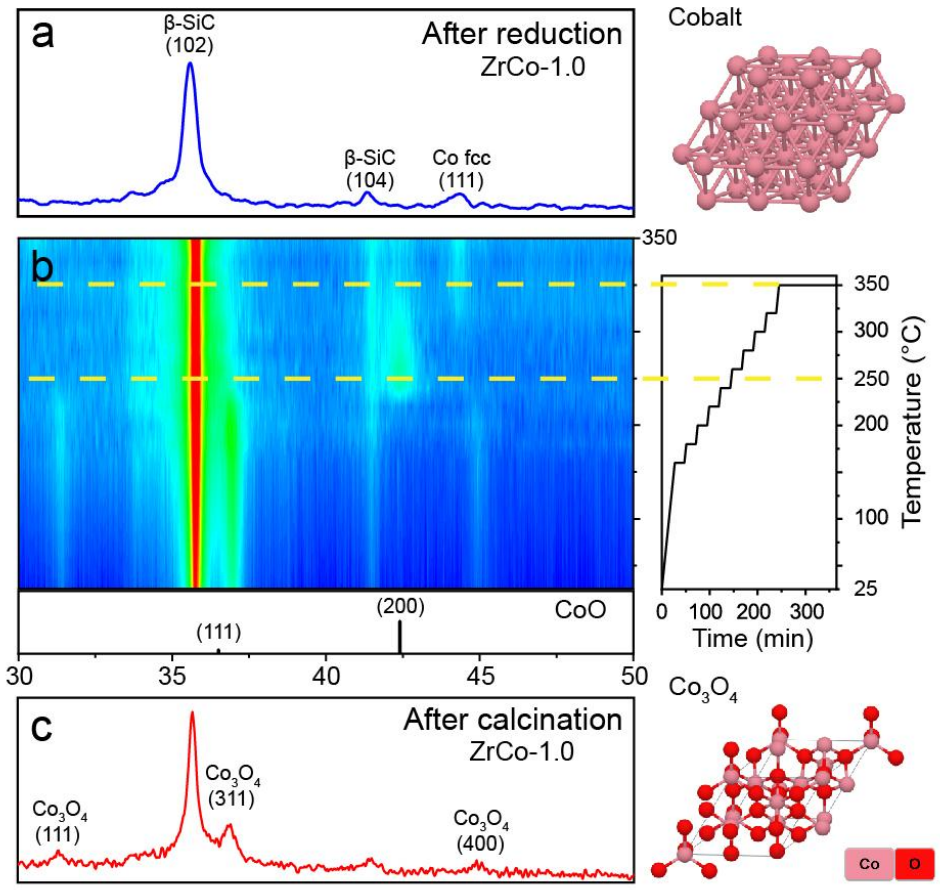

Figure 3. *In-situ* XRD experiments of ZrCo-1.0 catalyst. (a) Reduced ZrCo-1.0 catalyst, (b) XRD patterns of ZrCo-1.0 catalyst as function of reduction temperature under 30 mL min^{-1} H_2 at ambient pressure. (c) Calcined ZrCo-1.0 catalyst. The blue represents low intensity and red represents high intensity for the *in-situ* XRD patterns in (b).

The particle size of cobalt maintains similar value at the wide range of ZrO_2 addition, however, the ZrO_2 could influence the cobalt metallic surface area (MSA) due to the partial coverage on the cobalt surface.[16] Thus, it is interesting to investigate the relationship between the metallic cobalt surface area and the FTS catalytic activity. The cobalt surface MSA is recognized as the

place for CO and H_2 dissociation and also C-C coupling, which is an important factor to evaluate the FTS activity.[41-42] In this work, the cobalt MSA is determined by CO chemisorption (Figure 4a and Table 1) and its influence on the FTS activity has been analyzed. The MSA increases with the Zr/Co molar ratio from 0 to 0.5, reaching the maximum of 14 $m^2 \cdot g_{Co}^{-1}$ for ZrCo-0.5. When the ZrO_2 content is further increased, the MSA is sharply decreased. It is known that higher MSA means more Co active sites for FTS reaction[43] thus leading to superior catalytic activity. Surprisingly, the ZrCo-0.5 catalyst shows the highest MSA, whereas the highest CoTY is achieved by ZrCo-1.0 rather than the ZrCo-0.5, suggesting that MSA is not the sole influence factor for the catalytic performance.

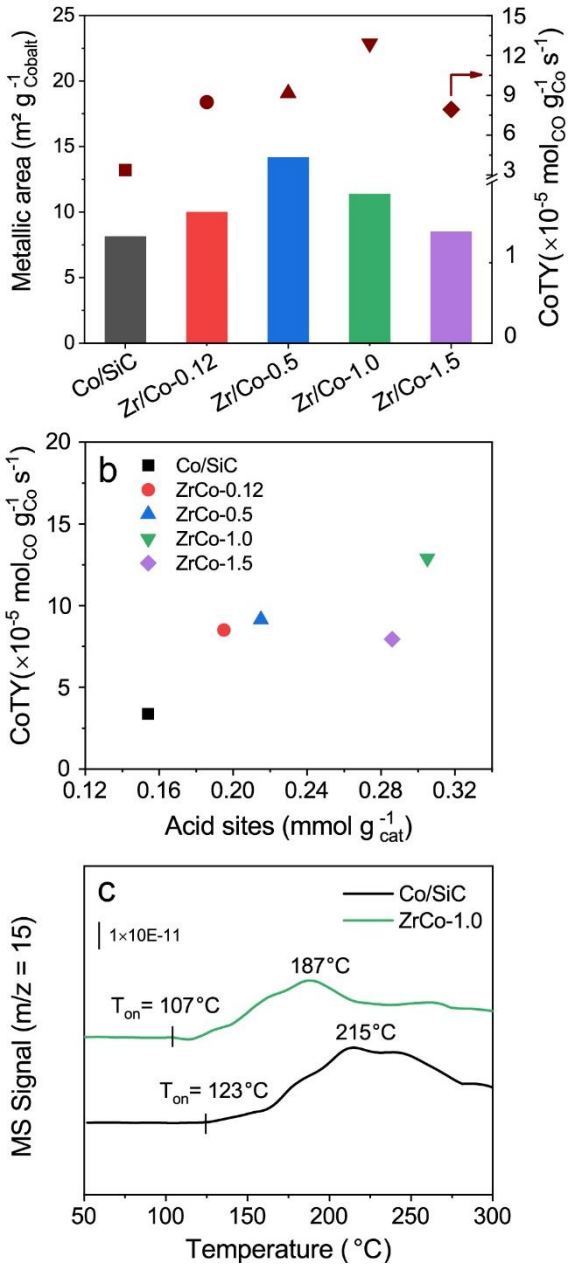

Figure 4. Metallic cobalt surface area (columns) determined by CO chemisorption and CoTY (red line) as a function of different Zr/Co molar ratio (a). The CoTY as a function of quantities of acid sites (b) for Co/β-SiC and Zr promoted ZrCo-x catalysts. CO-TPSR profiles (c) for Co/SiC and ZrCo-1.0.

In view of that ZrO_2 is amphoteric oxide that possess the acid property and basic property at the same time.[44] Previous results indicated that Lewis acid sites were beneficial for CO dissociation.[45] It might be ascribed to the stronger interaction between the O atom of adsorbed CO and the promoter that results in a weaker C-O bond that can be cleaved more readily. Similar mechanisms have been proposed for FTS over Co catalysts promoted with metal oxides[13]. Therefore, the acid property of the samples with different ZrO_2 content is also considered. NH_3-TPD measurements are carried out for the catalysts after reduction to evaluate the acidity of the catalysts. The ZrO_2 normally present acid sites of weak strength,[46] thus the desorbed NH_3 below 400° C is attributed to the weak acid sites on ZrO_2 and the NH_3 released above 400 ° C is ascribed to the strong interaction between NH_3 molecular and metallic cobalt surface.[19, 47] NH_3-TPD profiles (Figure S3) for Co/SiC and supported ZrCo-*x* catalysts reveal that the amount of acid sites increases with the Zr content in all catalysts except the ZrCo-1.0, which shows more acid sites than other samples. The amount of the acid site shows a positive effect on the CoTY (Figure 4b). The results imply that the presence of zirconia in ZrCo-*x* catalyst causes the enhancement in acidity and consequently influences the catalytic performance which is in agreement with current literature.[22, 48]

It is known that under the reaction condition the CO chemisorption on the catalyst surface is strong, and the coverage ratio is approximately unity, while the H_2 chemisorption is weak and its coverage is very low.[49] To further confirm the influence of Zr addition on CO adsorption and dissociation on the metallic cobalt surface,[50] the temperature dependent evolution of methane on behalf of the CO adsorption was monitored by CO-TPSR experiments.[51] To avoid interference

from the fragments of H_2O molecule, the m/z signal of 15 was monitered for methane. From the TPSR (Figure 4c), it shows that both the onset and the peaking temperature of methane for Zr promoted catalyst (ZrCo-1.0) are lower than the none-promoted one (Co/β-SiC). The fact that the Zr reduces the adsorption of CO, yielding the enhanced FTS performance is probably due to the Zr promotion of the CO dissociation. This agrees well with the reported literatures.[23-24]

Table 1. Physicochemical properties of various porous β-SiC supported ZrCo-*x* catalysts (Co loading=10 wt%).

Catalyst	Textural property [a]			Crystallite size [b]		Particle size [c]	CO-chemisorption		Reducibility[d] (%)
	S_{BET} ($m^2\ g^{-1}$)	Pore volume ($cm^3\ g^{-1}$)	Pore diameter (nm)	After calcination (Co_3O_4) (nm)	Used (Co^0) (nm)	Reduced (Co^0) (nm)	Metallic area (m^2/g_{Co})	D (%)	
Co/SiC	28	0.13	16.5	14.3	19.2	-	8.1	1.2	93.3
ZrCo-0.12	26	0.17	24.3	11.6	18.1	14	10.0	1.5	84.7
ZrCo-0.5	20	0.18	34.9	12.6	18.3	17	14.1	2.0	90.0
ZrCo-1.0	44	0.15	13.8	11.9	18.9	17	11.3	1.6	89.6
ZrCo-1.5	44	0.12	10.3	12.1	20.5	13	8.4	1.2	67.8
Co/ZrO_2	6	0.03	20.2	25.3	-	-	5.3	0.7	

a. BET profiles are shown in Figure S4.
b. Calculated from XRD
c. Determined from TEM
d. The degree of reduction is obtained by integrating the consumption peaks for H_2 which is shown in Figure S5.

Atomic resolution investigations of supported CoZr-*x* catalysts

Aberration-corrected HAADF-STEM was employed to explore the structure details of the ZrCo-*x* catalysts including the particle size, lattice spacing of grains and the status of Zr species. Figure 5 presents the atomic structure and elemental distribution of ZrCo-x catalysts via characterizations of atomic resolution HAADF-STEM imaging and EDS elemental mapping. It shows for the ZrCo-0.12 (Figure 5a-5c), the cobalt particles are in a core-shell configuration with a passivated oxide layer on the surface and Zr species are highly dispersed over the whole sample. The lattice fringes in spacings of 2.02 Å and 2.51 Å can be indexed to the (002) plane of fcc metallic cobalt phase and the (111) plane of β-SiC, respectively. Relatively bright contrast from strong scattering of Zr atoms in a HAADF imaging illustrates that Zr species exist in form of isolated atoms (labeled by purple circle) locating in both Co and β-SiC areas. To identify the distribution status of Zr species, the Zr/Co atomic ratios on the cobalt particle and the support are measured by EDS mapping (Figure S7). The results (Table S2) show a similar value of Zr/Co ratio for either an individual cobalt particle or the whole area containing both SiC support and cobalt particles. This suggests in the catalyst with low Zr content, Zr species are in homogeneous mono-dispersion on both the cobalt particle and support. The schematic illustration based on above structural analysis is given in Figure 5c.

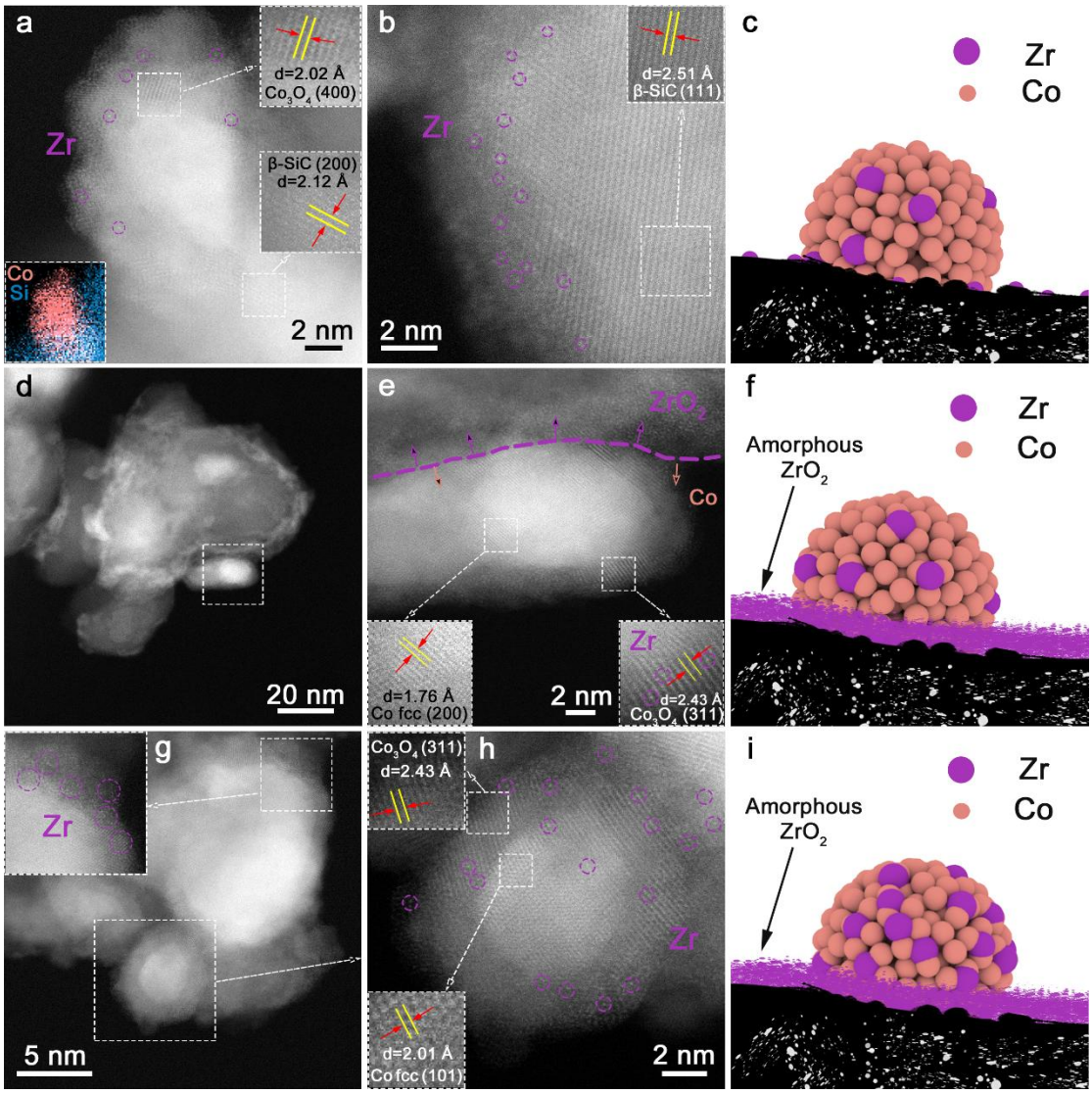

Figure 5. HAADF-STEM images for ZrCo-0.12 (a, b), ZrCo-0.5 (d, e), ZrCo-1.0 (g, h) catalysts and structural model (c, f, i) for each catalyst.

When promoting the Zr/Co molar ratio to be 0.5 via increasing the ZrO_2 concentration, microscopy results (Figure 5d) reveal that the surface of the β-SiC support is encapsulated with a bright layer that is recognized to be ZrO_2 species according to EDS elemental mapping evidence (Figure S8). Considering that there are no diffraction peaks in XRD patterns belonging to Zr species (Figure 2a), the ZrO_2 layer should exist in amorphous form, which could also be confirmed by the enlarged

STEM image of Figure 4e. Cobalt particle presents a Co_3O_4 oxidized layer with the thickness around 2 nm covering the metallic core of fcc cobalt. Distinguished from the situation on SiC support, Zr species on Co particle are highly dispersed without aggregation or forming coating layers. The EDS statistics (Table S3) as well as their corresponding STEM images (Figure S11) from three randomly selected regions disclose that Zr species preferentially concentrate on the surface of the SiC support leaving less Zr on Co particles. Such trend agrees well with microscopy observation (Figure 5d). Since Zr species accumulate on the support forming a layer outward, an interface between cobalt particle and Zr species shell appear as demonstrated by the EDS analysis (Figure S8). The above analysis concludes a structural illustration for ZrCo-0.5 as shown in Figure 5f, where the amorphous ZrO_2 covers on the support surface yielding the ZrO_2-Co interface, meanwhile those Zr species locating on Co particle distribute as single site promoters similar to the behavior in sample ZrCo-0.12.

Further increase the Zr/Co ratio to 1.0, partial Zr species remain oxide layer encapsulating on SiC supports (Figure S12), while the mono-dispersed Zr on cobalt particles becomes more abundant (Figure 5g, 5h) compared to the previous two catalysts ZrCo-0.12 and ZrCo-0.5. It is worth to be noticed that even the atomic ratio of Zr/Co is as high as 1.0, there is still no sign of ZrO_2 aggregations on the Co particles. The EDS and STEM evidences from multiple sample areas (Table S4 and Figure S12) reveal that Zr/Co atomic ratios for the support areas retain higher than those specific Co particles, which is analogous to the findings for catalyst ZrCo-0.5 as

illustrated by Figure 5i. Further quantitative data analysis will be discussed in section 4.2.

When the Zr content is consecutively increased reaching to the Zr/Co atomic ratio of 1.5 (Figure S13), it is intriguingly to find a distinct amorphous ZrO_2 layer outside the Co nanoparticle. Combined with aforesaid analysis from samples of all Zr/Co atomic ratios, we can draw brief conclusion that Zr species preferentially concentrate on the β-SiC support, while when the Zr additive exceeds a certain amount, the distribution on the Co surface would evolve from the isolated mono-dispersion into an continuous amorphous layer, which explains why the reaction activity of ZrCo-1.5 decreased compared with ZrCo-1.0. From the above results, a model can be established that the encapsulated amorphous ZrO_2 locates not only on the surface of the support but also on the Co nanoparticles, which is the cause for the large drop of the CoTY of the catalyst.

To investigate the chemical interaction of Co and Zr in atomic scale, the representative Co/SiC and ZrCo-1.0 catalysts were characterized by an environmental aberration corrected STEM (Hitachi HF5000) combined with the EELS analysis (Figure 6). The Zr $M_{4,5}$-edge EELS spectra of bulk ZrO_2 and CoZr alloy were also performed for better comparison. After *in-situ* reduction in the microscope of passivated catalyst, the cobalt oxide layer could be totally removed according to the EELS spectra of O K-edge (530 eV in Figure 6c) over Co/ SiC and ZrCo-1.0 catalysts. Consistent with the results of *ex-situ* STEM-HAADF analyses (Figure 5), the Zr species distribute into two different ways on the ZrCo-1.0 catalyst, one is coated on

SiC support (Figure 6a) and another is interacted with cobalt nanoparticle (Figure 6b). It is clearly shown that the bulk ZrO_2 presents the energy loss peak of 210 eV and 330 eV attributed to M_4 and M_3 edge for Zr and 530 eV owing to O K-edge. As shown in Figure 6c, the EELS spectra of Zr species on SiC and cobalt nanoparticles present the similar shape as bulk ZrO_2, revealing the Zr atoms not embedded into the cobalt lattice to form the alloy compound. The Co L-edge spectra of cobalt nanoparticles on Co/SiC and interacted with Zr on ZrCo-1.0 are selected to identify how the chemical interaction between Zr and Co (Figure 6d). It is known that the intensity ratio between the L_2 and L_3 edges is sensitive to the chemical valence for the cobalt species[52]. The L_3/L_2 ratio of ZrCo-1.0 catalyst is 1.47, which is much lower compared to that of Co/SiC catalyst (L_3/L_2 ratio of 1.88, Figure 6d). Such L_3/L_2 ratio decrement over ZrCo-1.0 catalyst probably attributed to the charge transfer from Zr species to Co nanoparticle, resulting in the more negative chemical valence for Co NPs (i.e. $Co^{\delta-}$ species in the surface of cobalt NPs).

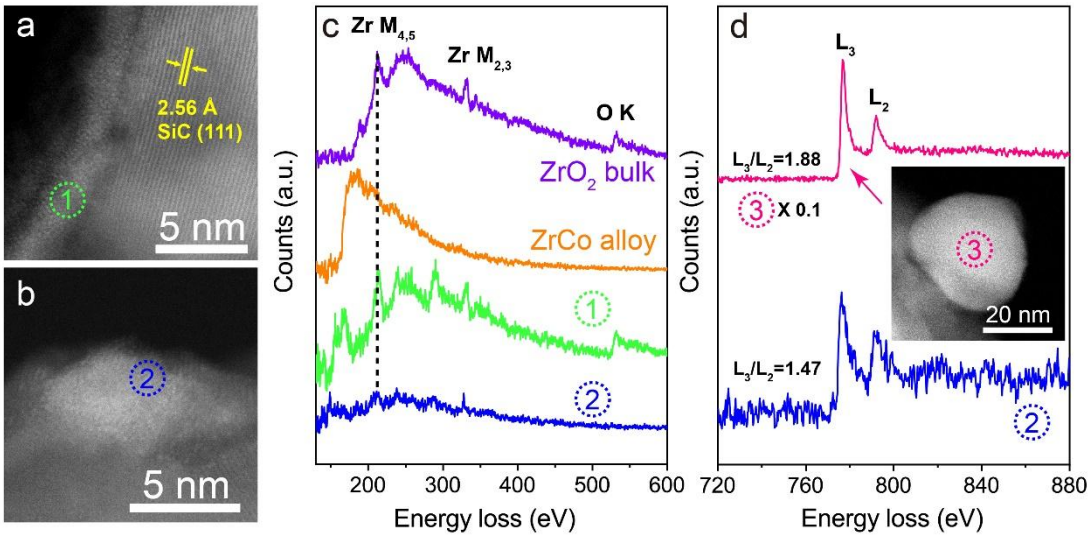

Figure 6. *In-situ* STEM experiments of Co/SiC and ZrCo-1.0 catalysts. Atomic resolution STEM-HAADF images of ZrCo-1.0 catalyst in the area with (a) ZrO_2 coated SiC and (b) ZrO_2 interacted with cobalt nanoparticles. (c) Zr M-edge EELS spectra for reduced ZrCo-1.0 with different locations, ZrO_2 bulk, and CoZr alloy. (d) Co L-edge EELS spectra for reduced Co/SiC and ZrCo-1.0 catalysts.

Discussion

4.1 Chemical structure of cobalt NPs in presence of Zr.

The cobalt particle size of the reduced ZrCo-*x* catalysts is about 10 nm according to the XRD and STEM characterizations (Figure 2 and Figure 5). The slightly larger appearance for particle size in sample ZrCo-1.5 is due to contribution of contrast overlay between the ZrO_2 layer and the Co core. In general, given the similar particle size, the surface area of Co NPs is expected to be also similar. However, the exposed MSA over the ZrCo-*x* catalysts shows remarkable variation illustrating a volcanic curve with maximum of 14.2 m^2/g for ZrCo-0.5 (Figure 4). Such MAS increment at lower ZrO_2 concentration mainly attributes to the rough surface of cobalt ascribed to introduction of isolated Zr species (Figure 4a). When the Zr/Co atomic ratio gets higher than 0.5 (ZrO_2 loading of 10 wt%), the amorphous ZrO_2 phase starts to accumulate over the cobalt surface that reduces the MSA meanwhile generates the ZrO_2-Co interface (Figures 5d-5i). The relative dense coverage of ZrO_2 amorphous layer in Zr/Co-1.5 catalyst leads to the worse FTS activity although it contains large amount of the Lewis acid sites (Figure 4b). According to the previous microscopy

results, two forms of Zr species have been identified on the Co NPs. The atomically isolated ZrO_2 at low ZrO_2 concentration and the amorphous ZrO_2 layer over Co surface at high ZrO_2 concentration. It can be found that the CoTY increases by 2.2 times from Co/SiC (3.7×10^{-5} $mol_{CO}g^{-1}_{Co}s^{-1}$) to ZrCo-0.12 ($8.5\times10^{-5}$ $mol_{CO}g^{-1}_{Co}s^{-1}$), but it only increases by 10% from ZrCo-0.12 to ZrCo-0.5 (CoTY of 9.2×10^{-5} $mol_{CO}g^{-1}_{Co}s^{-1}$). Such disproportion behavior indicates that not the amorphous ZrO_2 species but the isolated ZrO_2 sites on cobalt surface possess a dominant contribution to the CO dissociation.

To further understand the interaction between Zr species and cobalt nanoparticle, two more catalysts by the ZrO_2 pre-deposition over SiC support with the same Zr/Co molar ratio as ZrCo-1.0. As confirmed by XRD patterns in Figure S14, ZrO_2 presents as the amorphous state for Co@Zr_{350}-1.0, whereas displays well crystalline for Co@Zr_{650}-1.0. The interaction degree between cobalt and ZrO_2 could be labeled in the following order, ZrCo-1.0 > Co@Zr_{350}-1.0 > Co@Zr_{650}-1.0. It should be noted that, even the ZrO_2 was introduced on the support before cobalt, the single site Zr species could be not eliminated during the nucleation of Co NPs in calcination process as well as the reduction of metallic cobalt from the cobalt oxide. Such dramatic reconstruction of the bi-metallic nanoparticles during the reduction and reaction process was detected in our previous work[53]. However, lower interaction degree between Co and Zr could results in lower probability of single site of Zr species. It is clearly shown in Figure S15 that the FTS catalytic activity decrease

along with the decrement of the interaction efficiencies of between ZrO_2 and cobalt, which further confirm efficient active role of single-site Zr species.

4.2 Active sites at the atomic interface of Zr/Co.

To put insights into the interaction details of Zr and Co species, the atomic resolution STEM as well as the EDS characterization are employed to identify and quantify the characteristics of ZrO_2 promoter. To study the distribution variation between SiC support and Co NPs, two types of Zr content parameters have been focused (Figure 7a), the contents of the element averaged from a whole area (denoted as "A" for images), the contents of the element specialized from randomly selected Co NPs (denoted as "N" for images). All the data issues are from the statics over three randomly-selected areas/NPs and normalized using the mass percentage as shown in the Table S2 (10% ZrCo-0.12), Table S3 (10% ZrCo-0.5) and Table S4 (10% ZrCo-1.0). Their microscopy images correspond to Figures S10-S12, respectively. As shown in Figure 7b, the Zr/Co molar ratio on the Co NPs is 0.023 slightly lower than the whole area for the ZrCo-0.12 sample. Whereas the significant increment of Zr/Co molar ratio on the whole area compared to that on the individual Co NPs, indicating a clear tendency of preferential aggregation of ZrO_2 species on the support surface. The CoTY value for sample ZrCo-0.5 slightly increases compared to that of ZrCo-0.12, which is fitted well the same trend as the Zr/Co molar ratio on the individual cobalt NPs. For the catalyst ZrCo-1.0, the Zr/Co atomic ratio on the individual cobalt NPs is 5-7 times higher than that for the ZrCo-0.5 facilitating significantly promoted CoTY. Based on the data collected from the FTS performance, HAADF-STEM and EDS

analysis, it reaches a conclusion that the ZrO_2 species disperse on cobalt NPs are the real promoted sites that contribute to the improved FTS performance.

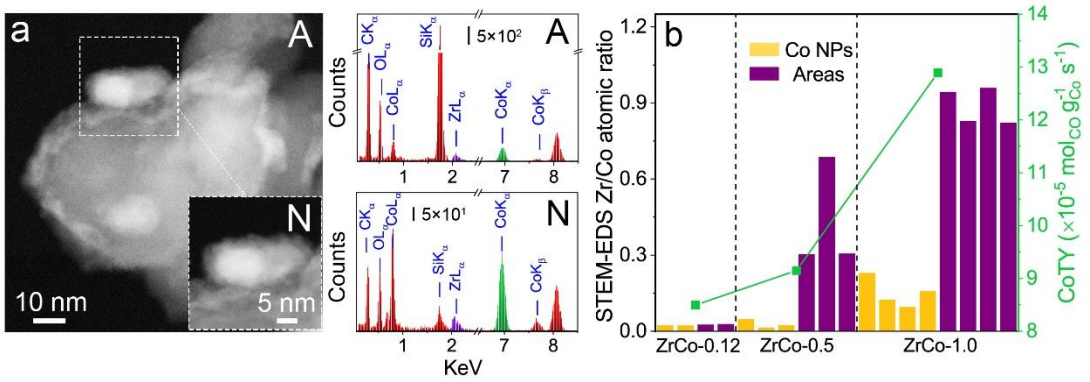

Figure 7. HAADF-STEM image with the corresponding EDS spectrum for different locations (a) and summarized Zr/Co atomic ratio for individual cobalt particles and areas (both cobalt particles and support included) with the overall CoTY for catalysts presented.

4.3 Theoretical investigations.

To understand the activity of FTS on different ZrCo-*x* catalytic surfaces, a previous volcano-like model was derived with the functions of adsorbate binding energies based on DFT calculations.[54] Notably, Co binds to adsorbates slightly weaker than the optimal activity as indicated from the volcano peak. In our study, DFT calculations were performed to evaluate: i) the promotion effect of Zr in catalysis and ii) the possible position of Zr when mixed with Co-catalysts (denoted as 'Zr-in-Co' for Zr atoms embedded in cobalt lattice; 'Zr-on-Co' for Zr atoms supported on cobalt surface). Therefore, the adsorption binding energies of H, C, and CO species were calculated on the surface of Co(111), Zr-in-Co(111), and Zr-on-Co(111), respectively

(Figure 8). Interestingly, it clearly demonstrates that Zr-in-Co(111) leads to very strong (*i.e.*, negative) binding energies for all the three adsorbates, indicative of the formation of hydride- or carbide-like materials. In contrast, the Zr-on-Co(111) surface has the H binding energy closer to that of Co(111).[55] The CO bindings on Zr-on-Co(111) is similar to that of Co(111), with the reason that CO tends to bind at the atop-site where the atomic ensemble effect is less predominant to tune the CO bindings.[56] This is also in excellent agreement with the XRD results that there was no significant shift of the cobalt oxides diffraction peaks induced by Zr doping (Figures 2 and 3). These results indicate that a Zr-on-Co(111) structure has the active site for C-C coupling and binding site of cobalt atoms to increase the FTS activity and selectivity in consistent with the experimental observations. Therefore, we suggest that Zr is not embedded into the lattice of Co; instead, it is expected to bind to the surface of Co NPs for the ZrCo-*x* catalysts. This is also in excellent agreement with the *in-situ* XRD results that there was no significant shift of the cobalt oxides diffraction peaks induced by Zr doping (Figure 3).

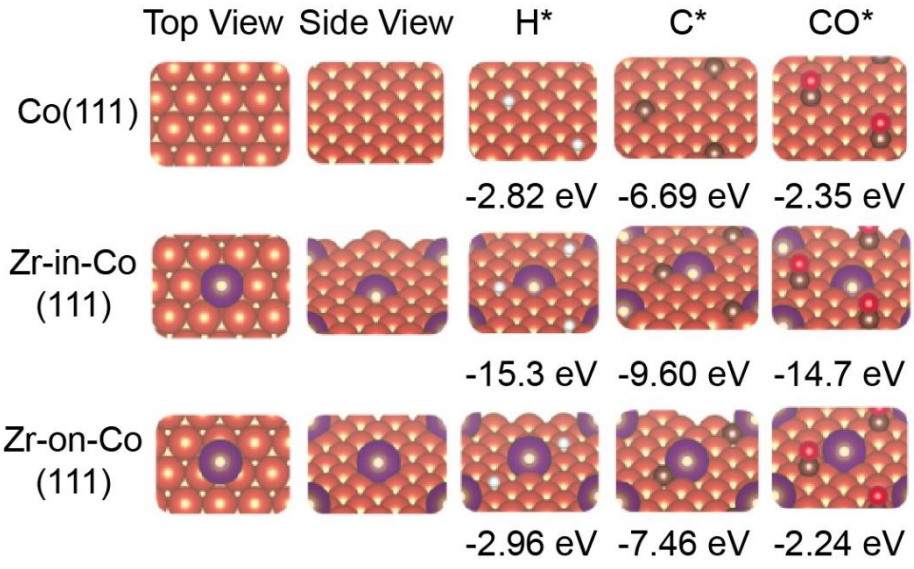

Figure 8. DFT-optimized configurations of H, C, and CO bindings on Co(111), Zr-in-Co(111), and Zr-on-Co(111) surfaces. Pink, purple, brown, red, and white spheres represent Co, Zr, C, O, and H atoms, respectively. "*" Represents an adsorption state.

The Zr promotion effect probably came from the combination of electronic and strain effects,[56] since the adsorption site (the surface ensemble) remained the same (Figure 8). Based on this comment, we carried out additional calculations to analyze the electron charge transfer and the bond length change at the Co sites after the doping of Zr (Table S5 and Figure S16). Interestingly, it can be clearly seen that doping of Zr on the Co (111) surface leads to the electron charge gain at surface Co (Figure S17), while it meanwhile leads to the enlarged Co-Co bond lengths. According to the *d*-band center theory[57], the charge gain of Co leads to the increase of Co *d*-band filling, which in turn down-shifts the *d*-band and weakens adsorbate bindings. But meanwhile, the enlarged average bond length tunes the adsorbate binding stronger due to the strain effect. From the enhanced binding strength of H and C at the Co sites (Figure 8), it is clear that the strain effect is predominant in determining the adsorbate binding after doping Zr onto Co (111). Such stronger bindings of H and C on Zr-on-Co(111) support that the Zr species act as the promoter that can strengthen the adsorbate bindings, which in turn promote the adsorption abilities of H_2 and intermediates of the products.[54]

The results presented in this work provide a new insight into the ZrO_2 promotion effects on the cobalt FTS catalyst. The single-site Zr species is revealed on the surface

of cobalt nanoparticle, as illustrated in Figure 9a. The single-site Zr species anchored on the surface of Co NPs and the charge is transferred from Zr species to Co nanoparticle. Thanks to charge transfer between Zr and Co atoms, the adsorbate binding with the H_2 molecule and the intermediate of the products are enhanced as well as beneficial for the CO dissociation during the FTS reaction. It thus enhances FTS catalytic activity and C_{5+} selectivity (Figure 9b) when the surface of cobalt NPs is not covered by ZrO_2. According to the previous reports that the increase of Zr content facilitates enhanced CO dissociation thus promoting CO conversion.[58-59] Therefore, under the promotion effect of Zr, it would be expected that the stronger binding of CO would decrease the ratio of H/CO on the catalyst surface, thereby enhancing the formation of C_{5+} products.

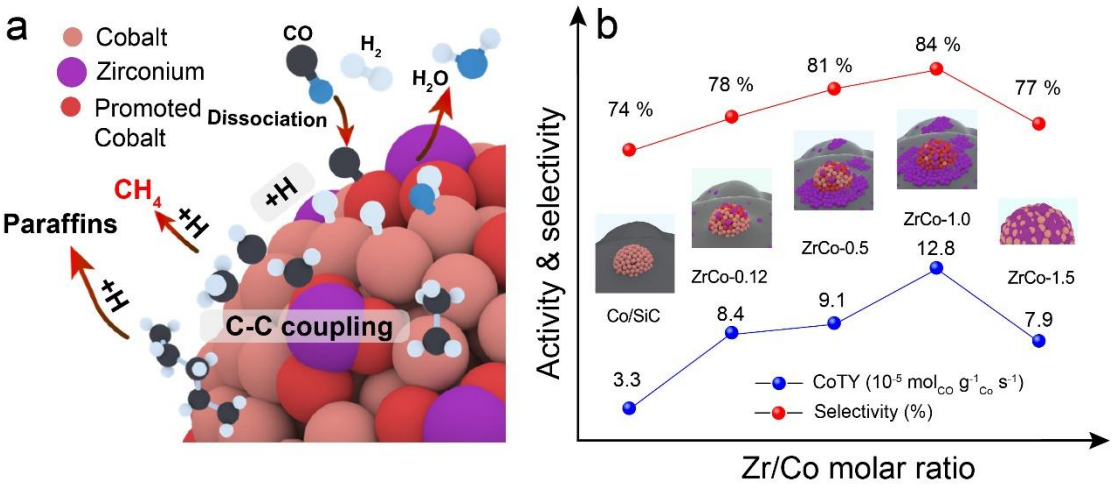

Figure 9. (a) Diagram illustrate the promotion effect of single site Zr anchored on the surface of Co nanoparticle. (b) The proposed structured models of ZrO_2 species

interacted with cobalt nanoparticle in virous of Zr/Co molar ratio and their tendency for the FTS catalytic activity and C_{5+} selectivity.

Conclusion

In this work, the promotion effect of ZrO_2 species on FTS performance of cobalt based catalysts has been explored on the basis of atomic structure analysis. The distribution of ZrO_2 species is clearly characterized by *in-situ*/*ex-situ* aberration-corrected STEM as well as EDS and EELS spectroscopy. For the samples with low Zr content, ZrO_2 locates on both cobalt particles and support in a mono-dispersion. With the increase of Zr content, it turns to concentrate on SiC support forming an amorphous coating layer directly contacting with the cobalt NPs, while further increasing Zr content (*e.g.*, 20 wt%) will result in the coverage of cobalt particle by ZrO_2 coating leading to the decreased activity. The improved activity was ascribed to the contribution to CO dissociation of metallic cobalt surface and Lewis acid sites. The optimal catalytic activity was obtained at the atomic ratio of ZrCo-1.0. Quantitative analysis on the Zr/Co ratio and corresponding CoTY discloses that the mono-dispersed ZrO_2 species on cobalt particle account for the promotion effect via providing enhanced CO dissociation ability.

Both of *in-situ* STEM-HAADF experiment combined with EELS and DFT theoretical simulation confirm that the obvious charge transfer occurs between single sites Zr species and Co NPs. Such stronger interaction between Zr species and cobalt NPs could also enhance the adsorbate binding with the H_2 molecule and the

intermediate of the products, which render the relative higher selectivity of long-chain hydrocarbons, i.e. 74% for ZrCo-1.0 and 84% for Co/β-SiC at similar CO conversion. The results provide an insight into the metal-promoter interaction in atomic scale and rethinking of promoter effects over the metal-catalyzed reaction.

ASSOCIATED CONTENT

Supporting Information.

Catalytic stability in iso-conversion, Product distribution, XRD patterns, N_2 adsorption-desorption isotherms, H_2-TPR profiles, NH_3-TPD profiles, HAADF-STEM and EDS images, benchmarking results, Normalized result of EDS, DFT results (Figure S1-S18, Table S1-S5) (PDF)

AUTHOR INFORMATION

Corresponding Author

*E-mail: weiliu@dicp.ac.cn (W. Liu), yuefeng.liu@dicp.ac.cn (Y. Liu), wangfei@hebut.edu.cn (F. Wang)

Author Contributions

The manuscript was written through contributions of all authors. All authors have given approval to the final version of the manuscript.

‡Y.P. and Q.J. contributed equally.

Notes

The authors declare no competing financial interest.

ACKNOWLEDGMENT

This work was financially supported from the National Natural Science Foundation of China (Nos. 51874115, 91645117, 21972140 and 21872144), Excellent Young Scientist Foundation of Hebei province, China (No. E2018202241), Enterprise Science and Technology Commissioner Project of Tianjin City, China (No. 19JCTPJC56100), CAS Youth Innovation Promotion Association (Nos. 2019190, 2018220), Liaoning Revitalization Talents Program (No.XLYC1907053), China Postdoctoral Science Foundation (No.2018M641726) and Talents Innovation Project of Dalian city (Nos. 2016RD04 and 2017RQ032). The authors acknowledge the SICAT Co. (www.sicatcatalyst.com) for providing porous β-SiC materials. Prof. Yunjie Ding and Dr. Ziang Zhao are acknowledged for the assistance of *in-situ* XRD experiment. We sincerely cherish our memory to Prof. Dang Sheng Su for his indispensable supports and fruitful discussions.

REFERENCES

1. Li, Z.; Ji, S.; Liu, Y.; Cao, X.; Tian, S.; Chen, Y.; Niu, Z.; Li, Y., *Chem Rev* **2019**.
2. Jia, J.; Qian, C.; Dong, Y.; Li, Y. F.; Wang, H.; Ghoussoub, M.; Butler, K. T.; Walsh, A.; Ozin, G. A., *Chem. Soc. Rev.* **2017,** 46 (15), 4631-4644.
3. Li, D.; Li, X.; Gong, J., *Chem. Rev.* **2016,** 116 (19), 11529-11653.
4. Zhong, L.; Yu, F.; An, Y.; Zhao, Y.; Sun, Y.; Li, Z.; Lin, T.; Lin, Y.; Qi, X.; Dai, Y., *Nature* **2016,** 538 (7623), 84-87.
5. Lin, L.; Zhou, W.; Gao, R.; Yao, S.; Zhang, X.; Xu, W.; Zheng, S.; Jiang, Z.; Yu, Q.; Li, Y.-W., *Nature* **2017,** 544 (7648), 80.
6. Borg, Ø.; Hammer, N.; Enger, B. C.; Myrstad, R.; Lindvåg, O. A.; Eri, S.;

Skagseth, T. H.; Rytter, E., *J. Catal.* **2011,** 279 (1), 163-173.
7. Shimura, K.; Miyazawa, T.; Hanaoka, T.; Hirata, S., *Appl. Catal., A* **2015,** 494, 1-11.
8. Cook, K. M.; Perez, H. D.; Bartholomew, C. H.; Hecker, W. C., *Appl. Catal., A* **2014,** 482, 275-286.
9. Khodakov, A. Y.; Chu, W.; Fongarland, P., *Chem Rev* **2007,** 107 (5), 1692-1744.
10. Tsakoumis, N. E.; Rønning, M.; Borg, Ø.; Rytter, E.; Holmen, A., *Catal. Today* **2010,** 154 (3-4), 162-182.
11. Tsubaki, N.; Sun, S.; Fujimoto, K., *J. Catal.* **2001,** 199 (2), 236-246.
12. Chu, W.; Chernavskii, P. A.; Gengembre, L.; Pankina, G. A.; Fongarland, P.; Khodakov, A. Y., *J. Catal.* **2007,** 252 (2), 215-230.
13. Johnson, G. R.; Bell, A. T., *Journal of catalysis* **2016,** 338, 250-264.
14. Morales, F.; de Groot, F. M.; Gijzeman, O. L.; Mens, A.; Stephan, O.; Weckhuysen, B. M., *J. Catal.* **2005,** 230 (2), 301-308.
15. Feltes, T. E.; Espinosa-Alonso, L.; de Smit, E.; D'Souza, L.; Meyer, R. J.; Weckhuysen, B. M.; Regalbuto, J. R., *J. Catal.* **2010,** 270 (1), 95-102.
16. Feller, A.; Claeys, M.; van Steen, E., *J. Catal.* **1999,** 185 (1), 120-130.
17. Moradi, G.; Basir, M.; Taeb, A.; Kiennemann, A., *Catal. Commun.* **2003,** 4 (1), 27-32.
18. Xiong, H.; Zhang, Y.; Liew, K.; Li, J., *J. Mol. Catal. A: Chem.* **2005,** 231 (1-2), 145-151.
19. Mu, S.; Li, D.; Hou, B.; Jia, L.; Chen, J.; Sun, Y., *Energy Fuels* **2010,** 24 (7), 3715-3718.
20. All, S.; Chen, B.; Goodwin, J., *J. Catal.* **1995,** 157 (1), 35-41.
21. Ma, W.-P.; Ding, Y.-J.; Lin, L.-W., *Ind. Eng. Chem. Res.* **2004,** 43 (10), 2391-2398.
22. Wu, Y.; Zhang, W.; Yang, M.; Zhao, Y.; Liu, Z.; Yan, J., *RSC Adv.* **2017,** 7 (39), 24157-24162.
23. Jongsomjit, B.; Panpranot, J.; Goodwin Jr, J. G., *J. Catal.* **2003,** 215 (1), 66-77.
24. Johnson, G. R.; Bell, A. T., *ACS Catal.* **2015,** 6 (1), 100-114.
25. Huang, X.; Teschner, D.; Dimitrakopoulou, M.; Fedorov, A.; Frank, B.; Kraehnert, R.; Rosowski, F.; Kaiser, H.; Schunk, S.; Kuretschka, C.; Schlogl, R.; Willinger, M. G.; Trunschke, A., *Angew Chem Int Edit* **2019,** 58 (26), 8709-8713.
26. Liu, Y.; Luo, J.; Shin, Y.; Moldovan, S.; Ersen, O.; Hébraud, A.; Schlatter, G.; Pham-Huu, C.; Meny, C., *Nat. Commun.* **2016,** 7, 11532.
27. Lunkenbein, T.; Schumann, J.; Behrens, M.; Schlögl, R.; Willinger, M. G., *Angew. Chem. Int. Ed.* **2015,** 54 (15), 4544-4548.
28. Su, D. S.; Zhang, B.; Schlögl, R., *Chem. Rev.* **2015,** 115 (8), 2818-2882.
29. Liu, Y.; Ersen, O.; Meny, C.; Luck, F.; Pham‐Huu, C., *ChemSusChem* **2014,** 7 (5), 1218-1239.
30. Duong-Viet, C.; Ba, H.; El-Berrichi, Z.; Nhut, J.-M.; Ledoux, M. J.; Liu, Y.; Pham-Huu, C., *New J. Chem.* **2016,** 40 (5), 4285-4299.
31. Liu, Y.; de Tymowski, B.; Vigneron, F.; Florea, I.; Ersen, O.; Meny, C.; Nguyen, P.; Pham, C.; Luck, F.; Pham-Huu, C., *ACS Catal* **2013,** 3 (3), 393-404.

32. de Tymowski, B.; Liu, Y.; Meny, C.; Lefèvre, C.; Begin, D.; Nguyen, P.; Pham, C.; Edouard, D.; Luck, F.; Pham-Huu, C., *Appl. Catal., A* **2012,** 419, 31-40.
33. Ba, H.; Liu, Y.; Mu, X.; Doh, W.-H.; Nhut, J.-M.; Granger, P.; Pham-Huu, C., *Appl. Catal., A* **2015,** 499, 217-226.
34. Liu, Y.; Florea, I.; Ersen, O.; Pham-Huu, C.; Meny, C., *Chem. Commun.* **2015,** 51 (1), 145-148.
35. Blöchl, P. E., *Physical review B* **1994,** 50 (24), 17953.
36. Perdew, J. P.; Burke, K.; Ernzerhof, M., *Phys. Rev. Lett.* **1996,** 77 (18), 3865.
37. Kohn, W.; Sham, L. J., *Physical review* **1965,** 140 (4A), A1133.
38. Monkhorst, H. J.; Pack, J. D., *Physical review B* **1976,** 13 (12), 5188.
39. Chen, C.; Wang, Q.; Wang, G.; Hou, B.; Jia, L.; Li, D., *The Journal of Physical Chemistry C* **2016,** 120 (17), 9132-9147.
40. Enache, D. I.; Rebours, B.; Roy-Auberger, M.; Revel, R., *J. Catal.* **2002,** 205 (2), 346-353.
41. Zhou, W.; Cheng, K.; Kang, J.; Zhou, C.; Subramanian, V.; Zhang, Q.; Wang, Y., *Chem. Soc. Rev.* **2019**.
42. Cheng, K.; Kang, J.; King, D. L.; Subramanian, V.; Zhou, C.; Zhang, Q.; Wang, Y. In *Advances in catalysis*, Elsevier: 2017; Vol. 60, pp 125-208.
43. Spadaro, L.; Arena, F.; Granados, M.; Ojeda, M.; Fierro, J.; Frusteri, F., *J. Catal.* **2005,** 234 (2), 451-462.
44. Albuquerque, E. M.; Borges, L. E.; Fraga, M. A.; Sievers, C., *ChemCatChem* **2017,** 9 (14), 2675-2683.
45. Boffa, A.; Lin, C.; Bell, A.; Somorjai, G. A., *Catal. Lett.* **1994,** 27 (3-4), 243-249.
46. Santiesteban, J.; Vartuli, J.; Han, S.; Bastian, R.; Chang, C., *J. Catal.* **1997,** 168 (2), 431-441.
47. Krishnan, C. K.; Hayashi, T.; Ogura, M., *Adv. Mater.* **2008,** 20 (11), 2131-2136.
48. Murata, K.; Okabe, K.; Inaba, M.; Takahara, I.; Liu, Y., *Catal. Lett.* **2009,** 128 (3-4), 343-348.
49. Van Der Laan, G. P.; Beenackers, A., *Catalysis Reviews* **1999,** 41 (3-4), 255-318.
50. Spivey, J. J.; Egbebi, A., *Chem. Soc. Rev.* **2007,** 36 (9), 1514-1528.
51. Fujimoto, K.; Kameyama, M.; Kunugi, T., *J. Catal.* **1980,** 61 (1), 7-14.
52. Xin, H. L.; Pach, E. A.; Diaz, R. E.; Stach, E. A.; Salmeron, M.; Zheng, H., *ACS nano* **2012,** 6 (5), 4241-4247.
53. Zhang, X.; Han, S.; Zhu, B.; Zhang, G.; Li, X.; Gao, Y.; Wu, Z.; Yang, B.; Liu, Y.; Baaziz, W., *Nature Catalysis* **2020**, 1-7.
54. Cheng, J.; Hu, P.; Ellis, P.; French, S.; Kelly, G.; Lok, C. M., *Top. Catal.* **2010,** 53 (5-6), 326-337.
55. Evans, E.; Li, H.; Yu, W.-Y.; Mullen, G.; Henkelman, G.; Mullins, C. B., *PCCP* **2017,** 19 (45), 30578-30589.
56. Li, H.; Shin, K.; Henkelman, G., *The Journal of chemical physics* **2018,** 149 (17), 174705.
57. Hammer, B.; Norskov, J. K., *Nature* **1995,** 376 (6537), 238-240.
58. Dinse, A.; Aigner, M.; Ulbrich, M.; Johnson, G. R.; Bell, A. T., *Journal of Catalysis* **2012,** 288, 104-114.

59. Den Breejen, J.; Radstake, P.; Bezemer, G.; Bitter, J.; Frøseth, V.; Holmen, A.; de Jong, K. d., *Journal of the American Chemical Society* **2009,** 131 (20), 7197-7203.